Ocean Modelling 72 (2013) 104–118

Contents lists available at ScienceDirect

Ocean Modelling

journal homepage: www.elsevier.com/locate/ocemod

Inference of turbulence parameters from a ROMS simulation using the k-ε closure scheme

Kristen M. Thyng [a,*], James J. Riley [a], Jim Thomson [b]

[a] University of Washington, Mechanical Engineering, Stevens Way, Box 352600, Seattle, WA 98195, United States
[b] Applied Physics Laboratory, University of Washington, 1013 NE 40th Street, Box 355640, Seattle, WA 98105-6698, United States

ARTICLE INFO

Article history:
Received 10 November 2012
Received in revised form 20 August 2013
Accepted 26 August 2013
Available online 6 September 2013

Keywords:
Turbulence modeling
ROMS
Kolmogorov theory
Tidal hydrokinetic energy
Puget Sound

ABSTRACT

Comparisons between high resolution turbulence data from Admiralty Inlet, WA (USA), and a 65-meter horizontal grid resolution simulation using the hydrostatic ocean modelling code, Regional Ocean Modeling System (ROMS), show that the model's k-ε turbulence closure scheme performs reasonably well. Turbulent dissipation rates and Reynolds stresses agree within a factor of two, on average. Turbulent kinetic energy (TKE) also agrees within a factor of two, but only for motions within the observed inertial sub-range of frequencies (i.e., classic approximately isotropic turbulence). TKE spectra from the observations indicate that there is significant energy at lower frequencies than the inertial sub-range; these scales are not captured by the model closure scheme nor the model grid resolution. To account for scales not present in the model, the inertial sub-range is extrapolated to lower frequencies and then integrated to obtain an inferred, diagnostic total TKE, with improved agreement with the observed total TKE. The realistic behavior of the dissipation rate and Reynolds stress, combined with the adjusted total TKE, imply that ROMS simulations can be used to understand and predict spatial and temporal variations in turbulence. The results are suggested for application to siting tidal current turbines.

1. Introduction

Oceanographic circulation models use turbulence closure schemes to represent processes at scales smaller than the resolution of the computational grid. Central to many of these schemes is Kolmogorov's theory for spectral energy transfer in three-dimensional turbulent flows, wherein energy is input into a flow at large scales and transferred to smaller scales. According to this theory, at and above some critical wavenumber, the spectral energy density in the system is approximately a function of only the wavenumber, the turbulent dissipation rate, and the viscosity. This region is called the equilibrium range and can be subdivided into two regions: the inertial subrange and the viscous subrange. In the inertial subrange, the energy can be interpreted as eddies which degenerate into eddies of smaller scale (or larger wavenumber), cascading the energy to smaller and smaller scales at the turbulent kinetic energy dissipation rate, ε, without the influences of viscosity. The spectral form of the inertial subrange is

$$k(\kappa) = \alpha\varepsilon^{2/3}\kappa^{-5/3}, \tag{1}$$

where k is the turbulent kinetic energy spectral density (also referred to as the TKE), κ is the horizontal wave number, and α is a universal constant whose approximate value has been found experimentally. The turbulence is three-dimensional in nature and the three components of the root-mean-square velocities are assumed to be isotropic in the inertial range. The viscous subrange is at higher wave numbers where viscosity becomes important, and in which energy is removed from the system at the turbulent dissipation rate.

Differences in the mixing predicted by various turbulence closure schemes have been shown by comparisons of model-predicted salinity along an estuary (*e.g.*, Warner et al. (2005a,b)). However, fewer comparisons can be found between model predictions and turbulence velocity data itself, partially due to the difficulty of obtaining the data. Two such studies, one of which was in a tidally-dominated flow, found reasonable comparisons for dissipation rate (Simpson et al., 2002; Stips et al., 2002). Another study in a shallow tidal estuary compared model predictions with data for Reynolds stresses, and found reasonable results (Wang et al., 2011). In a partially stratified estuary, Stacey et al. (1999) found a model over or underestimate of the TKE depending on the stratification. Here, we use a new set of turbulence comparisons from Admiralty Inlet, WA, to understand the performance of the turbulence closure scheme in the Regional Ocean Modeling System (ROMS), and to obtain more insight into the turbulence

* Corresponding author. Present address: Department of Oceanography, MS 3146, Texas A&M University, College Station, TX 77843-3146, United States. Tel.: +1 979 845 5472.
E-mail addresses: kthyng@tamu.edu (K.M. Thyng), rileyj@uw.edu (J.J. Riley), jthomson@apl.washington.edu (J. Thomson).

1463-5003/$ - see front matter © 2013 Elsevier Ltd. All rights reserved.
http://dx.doi.org/10.1016/j.ocemod.2013.08.008

dynamics. These comparisons focus on three parameters: turbulent kinetic energy, turbulent dissipation rate, and Reynolds stresses.

Admiralty Inlet is the main entrance to the Puget Sound, a fjord estuary in western Washington State. Admiralty Inlet has peak currents of over 3.5 m/s, depths between 50 and 180 meters, and is 5 km wide at the northern-most constriction (see Fig. 1). Dynamically interesting features are known to occur in the area, including the development of fronts (Thyng, 2012), tidal headland-generated eddies (Mofjeld and Larsen, 1984; Thyng, 2012), and areas of hydraulic control (Seim and Gregg, 1995). The large kinetic energy resource over a wide area makes Admiralty Inlet a strong candidate for tidal hydrokinetic power development (Polagye et al., 2007; Previsic et al., 2008; Haas et al., 2011; Kawase and Thyng, 2010).

A high level of turbulence is expected in Admiralty Inlet due to strong shear and periodic density variations in the water column. Turbulence is known to be a concern for turbine siting. In wind energy, many studies have examined turbulence as a cause of turbine failure (Frandsen, 2007; Madsen and Frandsen, 1984; Sheinman and Rosen, 1992; Thomsen and Sørensen, 1999; Wagner et al., 2010). Turbulence is known to decrease turbine efficiency as well as add additional stress onto the turbines (Sheinman and Rosen, 1992; Wagner et al., 2010). This has also been found to be the case with tidal turbines (Maganga et al., 2010). Results herein are proposed for use in selecting tidal turbine sites within Admiralty Inlet that have acceptable levels of turbulence.

2. Methodology

2.1. Field data

Multiple data sets of the currents in Admiralty Inlet were collected in 2011, as analyzed and discussed in Thomson et al. (2012). A set of acoustic wave and current (AWAC) data were gathered at a 56-meter-deep site near Admiralty Head from May to June 2011. One acoustic Doppler velocimeter (ADV) set and one acoustic Doppler current profiler (ADCP) set were gathered at a 22-meter-deep site near Nodule Point on Marrowstone Island in February 2011, for which period measurements indicated that stratification was not important during nonslack tides. Data locations are shown in Fig. 1. The ADV data were taken at a nominal turbine hub height of 4.7 meters above the seabed. They have less noise (error) in the measurements than the ADCP data, and are thus the most trusted source for comparison. The ADCP gives data

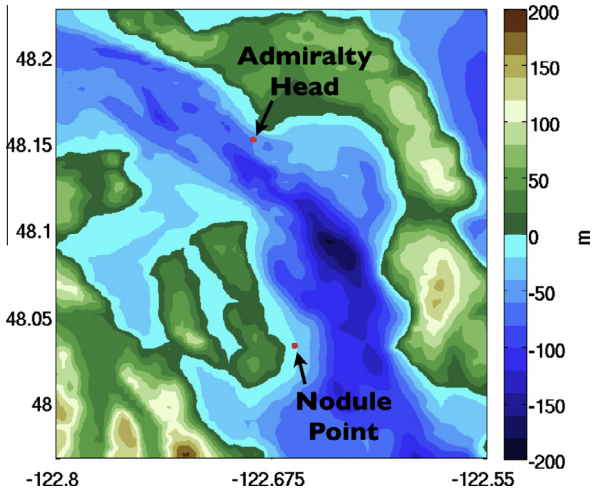

Fig. 1. Map of Admiralty Inlet with turbulence data locations indicated with red circles and colored contours showing bathymetry/topography in meters.

with height above the seabed, up to above 20 meters above the seabed. Note that ADCPs and AWACs are similar devices from different manufacturers and will here be generally referred to as ADCPs.

An additional ADV was deployed near Admiralty Head in June of 2012 to test the effectiveness of a new Tidal Turbulence Mooring, a method of suspending an ADV mid-water column using strongly heavy and buoyant attachments at the seabed and the top of the line, respectively, to hold the system nearly vertical (Thomson et al., 2013). This system is desirable for collecting high resolution ADV measurements at a depth that is pertinent to tidal hydrokinetic turbine deployment. Post-processing of the data is necessary to remove motion contamination. This will not be used as the primary data in this work, but will be used in the discussion in Section 5.

In order to use the ADCP data as well at the ADV data at Nodule Point, the ADCP data are "pinned" to the ADV data such that data taken at approximately the same height above the seabed by the two systems have approximately the same values for the turbulent kinetic energy and for the turbulent dissipation rate. In other words, to roughly account for the larger error present in the ADCP data, the ADCP data at Nodule Point are multiplied by a single factor (the ratio of the average value from the ADV over the average value from the ADCP at hub height) for the TKE and the dissipation rate (Reynolds stress is not calculated from the ADCP data) in order to match the hub height ADCP data to the hub height ADV data.

The data at are taken at sampling rates of 1 to 32 Hz, depending on the instrument, and processed using five minute windows, which was found in Thomson et al. (2012) to be the shortest time scale with a stable mean and variance in the data (i.e., stationarity). The processed data sets include five-minute running average estimates of speed (the mean flow), turbulent dissipation rate, and horizontal and vertical turbulent kinetic energy (referred to as TKE_{obs} for future differentiation) for both sites at hub height, as well as for a 20 meter profile above the seabed (from the ADCPs). In addition, the ADV set at Nodule Point is used to estimate turbulence spectra and Reynolds stresses.

The horizontal currents are rotated to be along and across the principal axis, which is defined for each averaging window separately. For each five minute averaging window, the mean flow pointing along (across) the principal axis is called u_p (v_p) and the velocity fluctuations, u'_p (v'_p), are taken as deviations around the mean flow in each direction. By design, the turbulent kinetic energy is largely contained along the principal axis. However, the energy contained in the perpendicular direction will also be considered because the model-predicted mean flow cannot be rotated to the same axes as the data, since the data is rotated for each five minute window and information from the model is output every fifteen simulation minutes. Both horizonal axes of information are included in comparisons in order to be as consistent as possible between the data and model. The relationship between the horizontal components of the TKE_{obs} at Nodule Point is used to infer the size of the across-axis component for the ADCP data sets, as $\sum(\overline{u'^2_p} + \overline{v'^2_p})/\sum \overline{u'^2_p} = 1.64$. This may be a low estimate for the relationship between v'_p and u'_p at Admiralty Head since the flow behavior there is different from the behavior at Nodule Point, with evidence that the TKE_{obs} in the directions of the principal axes are similar in size over a larger frequency range than at Nodule Point (see discussion in Section 5.1).

Turbulence spectra are calculated from the ADV data at Nodule Point using three overlapping sub-windows of 128 s, which are then averaged together to reduce confidence intervals in the five minute period analysis. Fig. 2 shows the time-averages of the TKE_{obs} spectra along and across the principal axis and along the vertical axis at Nodule Point from Thomson et al. (2012).

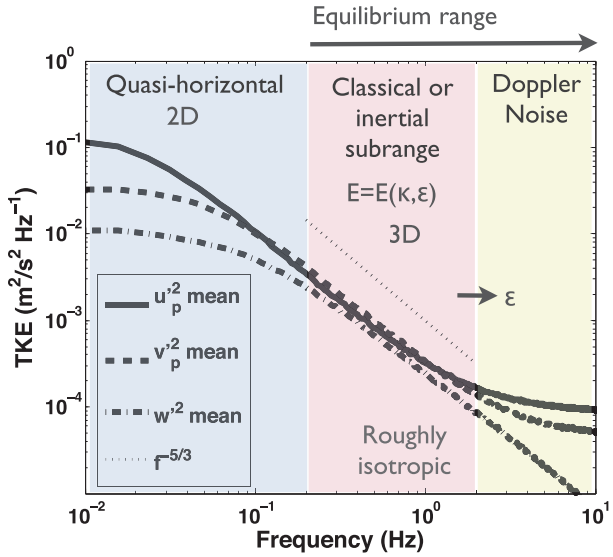

Fig. 2. Turbulent kinetic energy density along (solid) and across (dashed) the horizontal principal axis and the vertical axis (dash-dot) vs. frequency for data at Nodule Point at hub height of 4.7 meters. Individual occurrences of data in time spread around the mean half to a full order of magnitude but follow the same trend. Data during slack tide (when the mean flow is less than 0.8 m/s) are not included. Revised from Thomson et al. (2012), Fig. 8.

Also included in Fig. 2 is the theoretical form $f^{-5/3}$. This function is found by applying Taylor's frozen field approximation (Taylor, 1938), $L = u_p/f$, to Kolmogorov's theory (Eq. 1). In the approximation, the turbulence is assumed to be advected without distortion over the wavelength $L = 2\pi/\kappa$ at the mean speed of the horizontal motion, u_p.

The resulting form of Kolmogorov's spectra is:

$$\begin{aligned} k(\kappa) &= \alpha\varepsilon^{2/3}\kappa^{-5/3} \\ k(f) &= \alpha\varepsilon^{2/3}\left(\frac{2\pi f}{u_p}\right)^{-5/3} \\ k(f) &= \frac{\alpha}{(2\pi)^{5/3}}\varepsilon^{2/3}u_p^{5/3}f^{-5/3}. \end{aligned} \tag{2}$$

This theoretical form is consistent with TKE_{obs} density shown in the middle frequencies (0.2–2 Hz) of Fig. 2, where all three root-mean-squared components of the turbulent velocities are similar (i.e., demonstrating rough isotropy). This range of the frequency spectrum was defined in Thomson et al. (2012) as the region in which the vertical and horizontal TKE_{obs} were equivalent to each other, statistically, and to a universal $f^{-5/3}$. That is, there is no statistically significant difference at those frequencies between the spectral components or the fit itself. The turbulent kinetic energy in this range is found by integrating the TKE_{obs} spectral density data using values from only the frequencies in the range $0.2 < f < 2$ Hz and will be referred to as the *classical* TKE_{obs}.

At lower frequencies, below 0.1 Hz, Fig. 2 shows a distinct separation between the horizontal and vertical components of turbulent kinetic energy spectral density, with the along-principal ($u_p'^2$) component an order of magnitude larger than the vertical, and the across-principal ($v_p'^2$) component in between. This is indicative of highly anisotropic turbulence, where there is different behavior for horizontal and vertical motions, suggesting large, energetic, horizontal eddies dominating the energy. Energy may be input directly into the system at these, or larger, scales. This large scale turbulence is a significant portion of the *total* TKE_{obs}, which is defined as the integral of TKE_{obs} density over all frequencies.

At high frequencies, above 2 Hz, the horizontal TKE_{obs} becomes flat as result of Doppler noise (Thomson et al., 2012). The vertical component of the turbulent kinetic energy has less error and continues downward at about the same rate as in the middle frequency range. For ADV data, the noise is a very small fraction of the total TKE_{obs} and can be ignored.

From the Taylor frozen field approximation, the lower frequency range, from about 10^{-1} Hz to 10^{-2} Hz, corresponds to horizontal scales on the order of 10–100 meters. The water depth at Nodule Point is about 20 meters. In this frequency range the water depth becomes shallow compared to the horizontal scales of motion, which is probably the cause of the suppression of the vertical velocity in this range, resulting in the strong anisotropy in the kinetic energy components. Although the velocity field in this frequency range is quasi-horizontal, the flow is not two-dimensional since there is still strong variation in the vertical. We hypothesize that the vertical shearing of the quasi-horizontal motions leads to instabilities and turbulence at much smaller horizontal scales, where the vertical motion is not suppressed. This process results in a transfer of energy from the larger horizontal scales, where the motion is quasi-horizontal, to smaller horizontal scales, where the motion is classical, three-dimensional turbulence. We discuss more justifications of this hypothesis as well as its ramifications in Section 5.3.

2.2. Numerical model

The numerical simulation of Admiralty Inlet was run using the Regional Ocean Modeling System (ROMS) (Shchepetkin and McWilliams, 2005), using a k-ε turbulence closure scheme (Warner et al., 2005b). The equations of motion in ROMS are the set of primitive equations (Haidvogel et al., 2008; Shchepetkin and McWilliams, 2005). These are the Navier–Stokes equations with the hydrostatic and Boussinesq approximations. After decomposing the velocities, pressure, and scalar concentrations into a mean and fluctuation, *e.g.*, $u = \bar{u} + u'$, the equations are time-averaged in order to obtain a Reynolds-Averaged, Navier–Stokes (RANS) form. Note that throughout this document, the overbar is dropped from the mean properties. As an example, the equation for the u momentum is given as

$$\frac{\partial u}{\partial t} + \underline{v}\cdot\nabla u - fv = -\frac{\partial \phi}{\partial x} - \frac{\partial}{\partial z}\left(\overline{u'w'} - \nu\frac{\partial u}{\partial z}\right). \tag{3}$$

Here, $\underline{v} = (u, v, w)$ is the Cartesian mean velocity vector corresponding to the spatial coordinate vector (x, y, z) defined such that (x, y) gives the horizontal east–west and north–south position, and z the vertical position; $f(x, y)$ is the Coriolis parameter; ν is the molecular viscosity; $\phi(x, y, z, t)$ is the dynamic pressure with $\phi = p/\rho_0$; and ρ_0 is the background density. In the stress terms, u', v', w' are fluctuations about the mean and the overbar represents a time average.

The u-momentum equation is shown in Eq. 3 to indicate several features in the formulation of this model. The vertical turbulent diffusion is directly modeled (in the Reynolds stress terms) whereas the gradients in the horizontal direction are assumed to be small relative to other terms and are not considered. Although it is possible to do so in ROMS, horizontal mixing is not explicitly defined in this simulation, instead relying on the inherent numerical mixing to maintain numerical stability.

The Reynolds stress term in Eq. 3 is parameterized as

$$\overline{u'w'} = -K_M\frac{\partial u}{\partial z}. \tag{4}$$

The equations for the v-momentum stress term and for the turbulent tracer flux term are analogous to Eq. 4. K_M is the vertical eddy viscosity, whose form is given by

$$K_M = c\ell\sqrt{2k}S_M, \tag{5}$$

where c is a constant, ℓ is a turbulent length scale and S_M is a stability function of the local buoyancy and shear, and hence the local Richardson number, whose full form can be found in Warner et al. (2005b). Note that a principal effect of stable stratification in the model is to limit the turbulence length scale according to:

$$\ell^2 \leqslant \frac{0.56k}{N^2} \quad \text{for } N^2 > 0$$

as suggested by Galperin et al. (1988). These final terms are addressed in a turbulence closure scheme by determining the governing equations for the turbulent kinetic energy and length scale (or related turbulent quantity).

Most of the turbulence closure schemes available in ROMS use the generic length-scale framework (Umlauf and Burchard, 2003; Warner et al., 2005b). In this framework, well-known formulations are special cases of the generalized formulation and can be recovered using the appropriate constants. All of the formulations use a generic variable, ψ, to represent one turbulent field, which may be turbulent dissipation rate, ε, turbulent frequency, ω, or turbulent length scale, ℓ. The turbulent kinetic energy, k, is the other parameter used in these two-equation models and is defined by

$$k = \frac{1}{2}\left(\overline{u'^2} + \overline{v'^2} + \overline{w'^2}\right). \tag{6}$$

For the k-ε scheme used in this work, $\psi = \varepsilon$ and the turbulence closure scheme governing equations are given by

$$\frac{Dk}{Dt} = \frac{\partial}{\partial z}\left(\frac{K_M}{\sigma_k^\varepsilon}\frac{\partial k}{\partial z}\right) + P_s + P_B - \varepsilon \tag{7}$$

$$\frac{D\varepsilon}{Dt} = \frac{\partial}{\partial z}\left(\frac{K_M}{\sigma_\varepsilon}\frac{\partial \varepsilon}{\partial z}\right) + \frac{\varepsilon}{k}(c_{\varepsilon 1}P_s + c_{\varepsilon 3}P_B - c_{\varepsilon 2}\varepsilon), \tag{8}$$

where P_s is the shear production, P_B is the buoyancy production, and σ_k^ε and σ_ε are the Schmidt numbers for the eddy diffusivity of turbulent kinetic energy and dissipation rate, respectively. The forms for the production terms are given as

$$P_s = -\overline{u'w'}\frac{\partial u}{\partial z} - \overline{v'w'}\frac{\partial v}{\partial z} = K_M M^2, \quad M^2 = \left(\frac{\partial u}{\partial z}\right)^2 + \left(\frac{\partial v}{\partial z}\right)^2 \tag{9}$$

$$P_B = -\frac{g}{\rho_0}\overline{\rho' w'} = -K_C N^2, \quad N^2 = -\frac{g}{\rho_0}\frac{\partial \rho}{\partial z}, \tag{10}$$

with ρ the density which is dependent on pressure, temperature, and salinity; K_C the vertical eddy diffusivity, which has an analogous form to K_M given in Eq. 5; and N the buoyancy frequency. The constant values are $\sigma_k^\varepsilon = 1.0, \sigma_\varepsilon = 1.3, c_{\varepsilon 1} = 1.44, c_{\varepsilon 2} = 1.92$, and $c_{\varepsilon 3} = \pm 1.0$.

2.3. Numerical simulation

The numerical simulation described in this study was run in ROMS with 65 meter horizontal resolution and 20 evenly-spaced vertical layers for the month of September in 2006, using a k-ε turbulence closure scheme. This high resolution simulation is nested inside a larger regional model of the inland waterways of western Washington and the northeast corner of the Pacific Ocean, which is described in Sutherland et al. (2011). The time step of the Admiralty Inlet simulation was 5 s and model fields were output every 15 min. The minimum vertical layer thickness is 0.2 meters, occurring at points that have the minimum depth allowed in the simulation of 4 meters, and the maximum thickness is about 9.3 meters and occurs where the domain is deepest (about 180 meters). The bathymetry has been smoothed such that

$$r_0 = \max\left(\frac{H_i - H_{i-1}}{H_i + H_{i-1}}\right) \approx 0.2$$

for neighboring cells in water columns of depth H_i and H_{i-1} (Beckmann and Haidvogel, 1993), and

$$r_1 = \max\left(\frac{z_{i,k} - z_{i-1,k} + z_{i,k-1} - z_{i-1,k-1}}{z_{i,k} + z_{i-1,k} - z_{i,k-1} - z_{i-1,k-1}}\right) \approx 7.6,$$

for the vertical location z for neighboring points i and $i-1$ and vertical levels k and $k-1$ (Haney, 1991). The open boundary conditions used for physical forcing are the Flather boundary condition for depth-averaged (barotropic) velocity, the Chapman boundary condition for free surface, radiation and nudging for the 3D (baroclinic) velocity, and for radiation with nudging for the tracer condition. A no-slip boundary condition is used at vertical walls and quadratic bottom stress is employed at the seabed with $C_D = 3 \times 10^{-3}$, a typical value that was also used in the regional forcing model and was found to not significantly affect model results when varied by orders of magnitude (Sutherland et al., 2011).

The model performs reasonably well in many metrics and is described in detail in Thyng (2012). Physically, eddies generated by Admiralty Head appeared to be captured in the model when compared with shipboard ADCP data (NNMREC, University of Washington, 2010). The model and data have good agreement in the location of the sharp horizontal speed, horizontal direction, and vertical velocity gradients seen at the outer edge of the eddy, though the speed is lower in the model than in the data.

When harmonically decomposed, the free surface M_2 amplitudes are consistently low by close to 25%. The tidal phase propagation through the model domain is correct, which is related to dissipation and is important dynamically (Mofjeld and Larsen, 1984). M_2 velocity constants are also approximately 75% the size of the values from the field data. For the time periods compared in this study, the full horizontal speed signal (with all tidal constituents included) is on average about 25% low. These are known problems in the larger forcing regional model, and are inherited by this nested model. The effect of the deficiency in the speed on the turbulence parameters is discussed in Section 5.2.

2.4. Alignment of data and model time series

The timing of the simulation run, September 2006, does not coincide with any of the turbulence field data sets, which are from 2011. However, for the tidally-driven phenomena of interest, select tidal cycles from the 2006 model simulation can be compared with the 2011 data. The following approach aligns non-coincident data sets for comparison.

A straight-forward and physically-based approach is to align time series based on their free surface signals at a specific location. Simulations indicate that the free surface elevation range covered during a half-cycle duration correlate with many of the flow features in the system. Using consecutive similarly-sized half-cycles (by the measures of range and duration) between the data and model free surface signals, we can make realistic comparisons between the data and model flow fields. Fig. 3 shows an example of aligned time series. This method is used to find appropriate model output for comparison with the Nodule Point and Admiralty Head data sets. The duration of the comparison time is different for the two data sets since they were obtained at different times and is for as many consecutive tidal phases as could be reasonably aligned.

2.5. Turbulence parameters

Expressions used to calculate turbulent properties from the field velocity data can be found in Thomson et al. (2012). This section details the expressions used for the model output, given parameterizations used in the simulation (shown in Section 2.2).

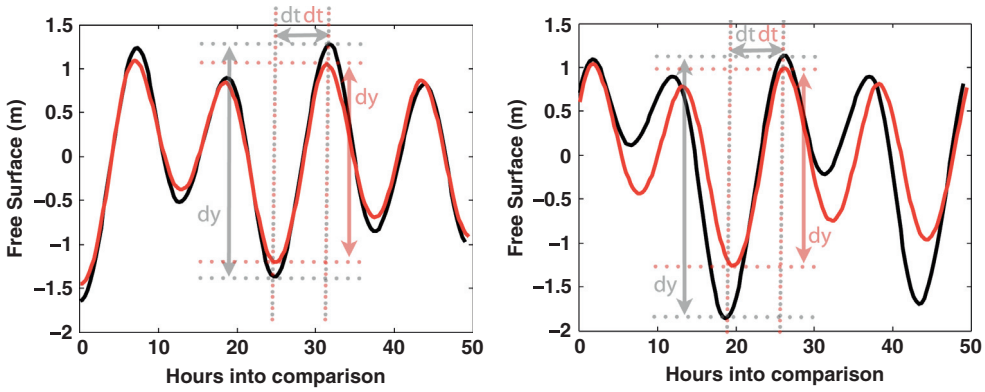

(a) Decent alignment between two series (b) Poor alignment between two series

Fig. 3. Time series information from non-coincident times are aligned by finding consecutive half-cycles with similar range and duration between the free surface signals at the same location from each time series. Fig. 3(a) shows two signals with comparable range and duration for a flood tide from about 24 to 30 h into the comparison. The tides around the marked tide are also decent matches, such that the series of consecutive tidal phases may be aligned to find a reasonable comparison for fields from the sources and times represented by the two signals. In Fig. 3(b), the duration for the marked flood (from about 20 to 26 h into the comparison) is similar, but the range is too different to make a meaningful comparison, indicating that the system behavior and characteristics during the cycles may be very different from each other.

Turbulent kinetic energy from the model is compared with data either with only horizontal and with both horizontal and vertical components (as noted in figure captions). The turbulent kinetic energy, k, from the model, by design, includes all three components and is approximately isotropic, so horizontal-only kinetic energy from the model is represented as $2/3k$. This field is directly output by the numerical simulation and will be referred to as the TKE_{model}.

The effect of turbulence on a turbine is typically calculated using the turbulence intensity metric used in wind energy analysis. This metric is given by the turbulent velocity fluctuations divided by the mean velocity. In the field data analysis, this is calculated for the principal horizontal velocity fluctuation component. For model output, the turbulent fluctuation, or the root-mean-square fluctuating velocity, is found in terms of turbulent kinetic energy, the quantity output from the turbulence closure scheme: $k = \frac{1}{2}\left(\overline{u'^2} + \overline{v'^2} + \overline{w'^2}\right) \approx \frac{3}{2}\overline{u'^2}$, so $\overline{u'^2} \approx \frac{2k}{3}$. A turbine rotor face would encounter a single directional component of turbulence intensity, and the model output turbulent kinetic energy has no directional preference. Therefore, for the model output, the turbulence intensity is calculated as

$$I = \frac{\sqrt{\overline{u'^2}}}{\sqrt{u^2 + v^2}} \approx \frac{\sqrt{2k/3}}{\sqrt{u^2 + v^2}}.$$

Both components of horizontal velocity are used in the denominator of this calculation despite one component being represented in the numerator due to the arbitrariness of the velocity vector direction relative to the principal axis direction. It may be an over-estimation to use the magnitude of the full horizontal tide, but it is preferable to using a single velocity component, which may or may not represent the prevalent tidal flow direction. In presentation of turbulence intensity, values corresponding to currents below the cut-in speed are removed because the turbines will not respond to these low speeds. A cut-in speed of 0.8 m/s is used for this purpose for both the field data and model analysis (Thomson et al., 2012).

The Reynolds stress component for the principal axis horizontal direction and the vertical direction, $\overline{u'w'}$, is given in the Nodule Point ADV data set. For the model output, the magnitude of the two components of the Reynolds stress tensor, $\overline{u'w'}$ and $\overline{v'w'}$, are calculated using the parameterization in ROMS (Eq. 4) and and combined for comparison with the principal axis data as

$$\text{Reynolds stress}_{\text{model}} = \sqrt{\overline{u'w'}^2 + \overline{v'w'}^2}$$
$$= K_M \sqrt{\left(\frac{\partial u}{\partial z}\right)^2 + \left(\frac{\partial v}{\partial z}\right)^2}.$$

The parameterizations of the shear and buoyancy production terms for ROMS model output were given in Eqs. 9 and 10.

The rate of turbulent kinetic energy dissipation, ε, is directly output from the model. From the field data, ε is calculated from the ADV spectra as well as from the structure function of the ADCP profiles.

3. Results

3.1. Nodule Point comparison

A comparison over about 2 days or 4 tidal cycles of turbulence data with model output at hub height at Nodule Point is shown in Fig. 4. Fig. 4(a) shows the free surface agreement for two non-coincident time series (Section 2.4). The mean speed (b), turbulent dissipation rate (d), and Reynolds stress (e) in the field data and model output are in reasonable agreement, especially considering the uncertainty of turbulence modeling (Pope, 2000). The model horizontal speed is close to 25% low, as previously stated, and the latter two turbulence parameter model predictions are each within a factor of two of the field data, on average.

The turbulent kinetic energy (Fig. 4(c)), however, does not compare as well; the total TKE_{obs} from the field data is approximately three times larger than in the model simulations. The large discrepancy in the comparison of total turbulent kinetic energy shown between the black and red lines in Fig. 4 may result from the fact that field data includes length scales larger (or frequencies lower) than what is included in the ROMS turbulence closure scheme. For example, frequencies between 10^{-2} and 10^{-1} s^{-1}, which are included in the data turbulent averaging window, correspond roughly to length scales of 100 and 10 meters, respectively. These are too large to be considered classical turbulence, especially given the very strong anisotropy in the kinetic energies shown in Fig. 2. Because of this, a better comparison between the data and the turbulence model, which is intended to model classical turbulence, is to restrict the turbulent kinetic energy data to frequencies in the classical range.

Following the frequency classifications of the data suggested in Fig. 2 and described in Section 2.1, the total turbulent kinetic energy observed in the field can be split into two main parts: the anisotropic lower frequency motions, and the roughly isotropic (classical) higher frequency motions. As shown in Fig. 5, the model output, TKE_{model}, compares favorably with the classical TKE_{obs}. This improved matching of the classical TKE_{obs} is also shown in Fig. 4 with the classical TKE_{obs} in blue. Note that the frequency cutoff

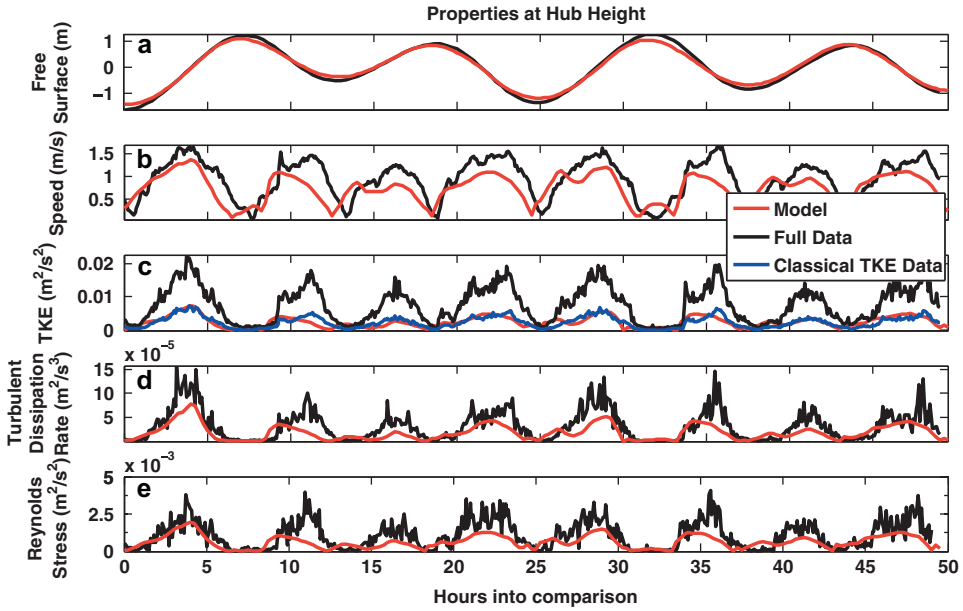

Fig. 4. Turbulence comparison between data (black) and model (red) at hub height of 4.7 meters at Nodule Point. Both model and data turbulent kinetic energy include vertical and horizontal components. The classical TKE_{obs} is shown in blue and matches better with the model output. (For interpretation of the references to colour in this figure caption, the reader is referred to the web version of this article.)

used to separate out the classical TKE_{obs} from the rest of the TKE_{obs} was not a varied parameter (Section 2.1).

The results for the turbulent dissipation rate with depth at Nodule Point are shown in Fig. 6. The bottommost comparison (Fig. 6(d)) is approximately at hub height and shows good agreement, as was also shown with the ADV data (Fig. 4). Both the model and the observational estimates decrease with increasing distance above the seabed, however the data decrease more sharply. The depths of the time series comparisons are indicated in the time-average of the dissipation rate (Fig. 6(e)).

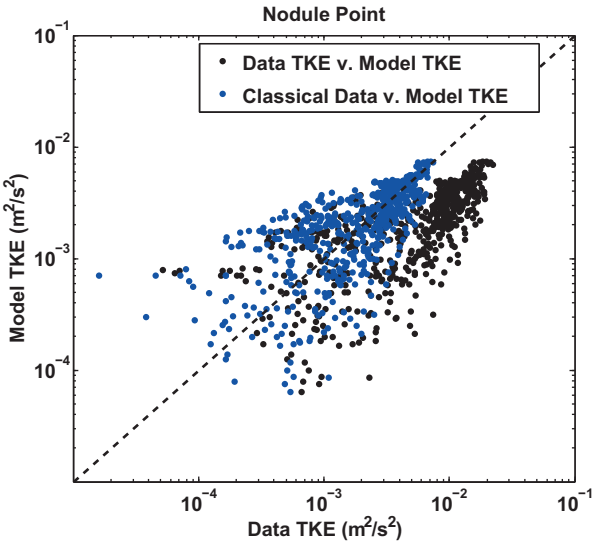

Fig. 5. Hub height 1–1 comparisons of TKE_{model} and types of TKE_{obs} at Nodule Point. Black shows TKE_{model} compared with the full TKE_{obs}. Blue shows the TKE_{model} compared with the TKE_{obs} taken only over the classical turbulence frequency range. Both model and data turbulent kinetic energy include vertical and horizontal components.

3.2. Admiralty Head comparison

Comparisons over 3.5 tidal cycles of turbulence quantities at Admiralty Head are shown in Fig. 7. The alignment in the data and model time series is not as good as in the Nodule Point case, as shown in the more pronounced mismatch in the free surface signal (Fig. 7(a)). The comparisons are reasonable between the model output and data, in particular the agreement of dissipation rate (d) which is within a factor of two on average. The total turbulent kinetic energy (c) from the model output is lower than from the data set, but not as low as the total at Nodule Point. This difference in behavior is discussed in Section 5.1.

Comparisons for the turbulent dissipation rate at Admiralty Head with depth are given in Fig. 8. Shown in Fig. 8(a–d) is data-model comparisons for the same time period shown in Fig. 7, but at various depths. These depths are indicated in Fig. 8(e) of the time-average of the dissipation rates over the comparison period. The model and the observational estimates agree well, and both decrease with increasing distance from the seabed.

3.3. TKE Budget comparison

The production and dissipation of TKE are examined using the ADV data at Nodule Point and using the model at both sites. In energetic tidal flows, shear production is expected to roughly balance with dissipation. Fig. 9 shows two one-to-one log–log plots of shear production versus the turbulent dissipation rate for the data and model output. The spread in the data is much larger than in the model output. This spread was interpreted in Thomson et al. (2012) as indicating important turbulent kinetic energy transport at the location due to eddies shedding from the headland. Instrument noise also contributes to the spread. While both data and model predictions line up somewhat along the one-to-one dotted line, the model output does not show the same scatter at larger values.

In addition to shear, buoyancy is a source (or sink) of TKE (see Eq. 7). Buoyancy production is positive in unstable stratification and negative in stable stratified flows. In these simulations, the buoyancy production is almost always negative, which means that

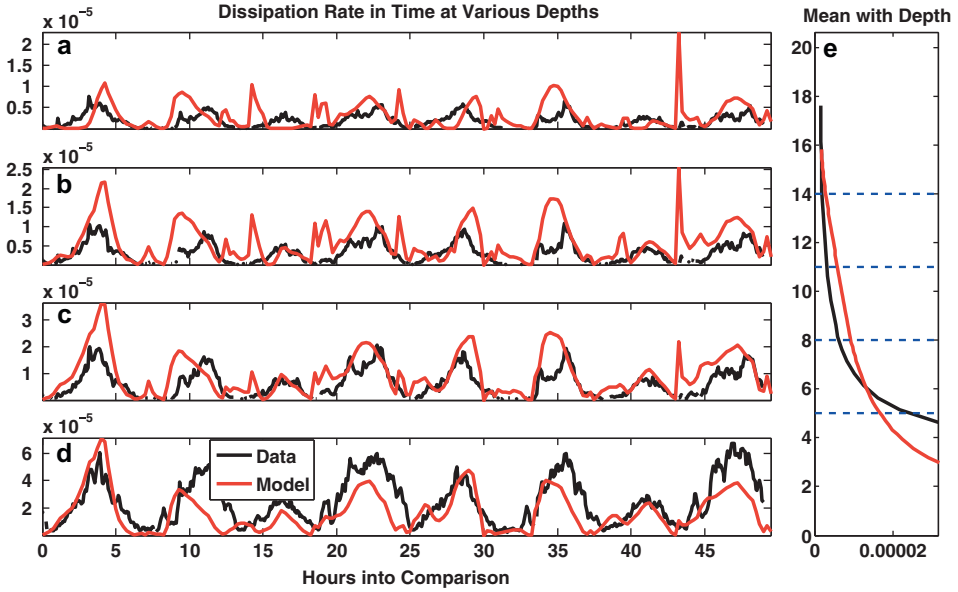

Fig. 6. Turbulent dissipation rate comparisons between data (black) and model (red) at Nodule Point for the same time periods as Fig. 4 but at multiple depths (Fig. 6(a–d)). The comparison depths are indicated, in order, as blue dashed lines on the time-mean profile of the turbulent dissipation rate profiles in Fig. 6(e). The ADCP data have been pinned to the ADV data at hub height (d) as described in Section 2.1. (For interpretation of the references to colour in this figure caption, the reader is referred to the web version of this article.)

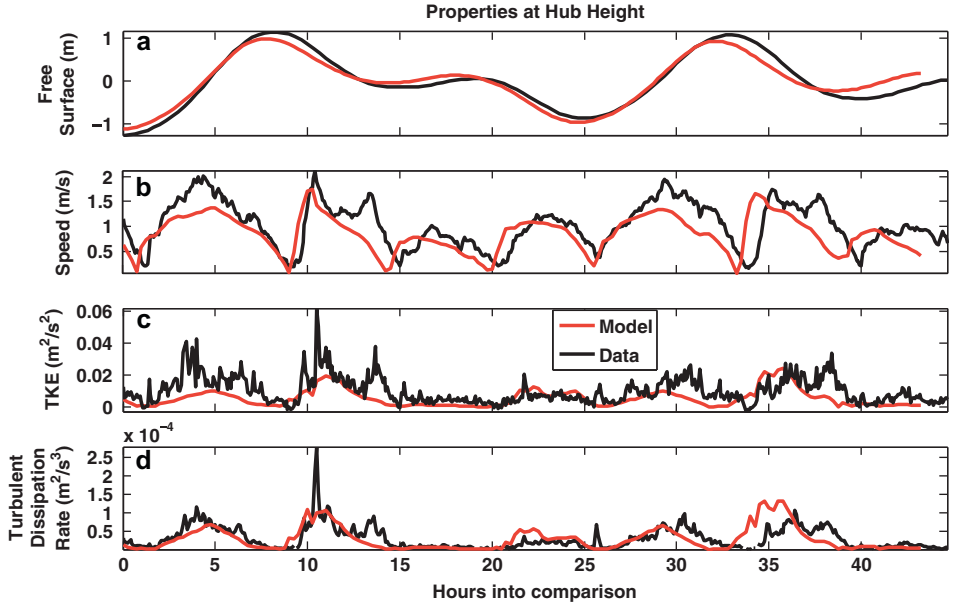

Fig. 7. Turbulence comparison between data (black) and model (red) at hub height of 8.1 meters at Admiralty Head. Both model and data turbulent kinetic energy include vertical and horizontal components. (For interpretation of the references to colour in this figure caption, the reader is referred to the web version of this article.)

the mean density profile is almost always stable. In the case of stable stratified flows, P_B is a sink for the turbulent kinetic energy and a source for the available potential energy. In other words, the effect of buoyancy in the turbulence closure scheme is to produce a loss of kinetic energy to background mixing.

Fig. 10 shows the relative size of the shear production term and the buoyancy production term from the model simulations at both Admiralty Head and Nodule Point. At both locations, the shear production dominates the buoyancy production, except at low values, where buoyancy production becomes important. Buoyancy production may dominate when there is less energy in the system because when the speed is lower, the ratio of the buoyancy force to the inertial force is larger (as seen in the Richardson number). There is more spread in the comparison at Admiralty Head than at Nodule Point, perhaps indicative of the more active eddy field (and more TKE transport) at Admiralty Head. Both sites show a further preference toward shear production nearer the seabed, moving closer to the one-to-one line away from the seabed. This is indicative of the bottom friction near the seabed generating more shear.

The "tail" seen in Figs. 9 and 10 indicates a minimum value in the turbulent dissipation rate and the buoyancy production, but not in the shear production. The limitation is imposed in order to restrict mixing in stable stratification (Warner et al., 2005b).

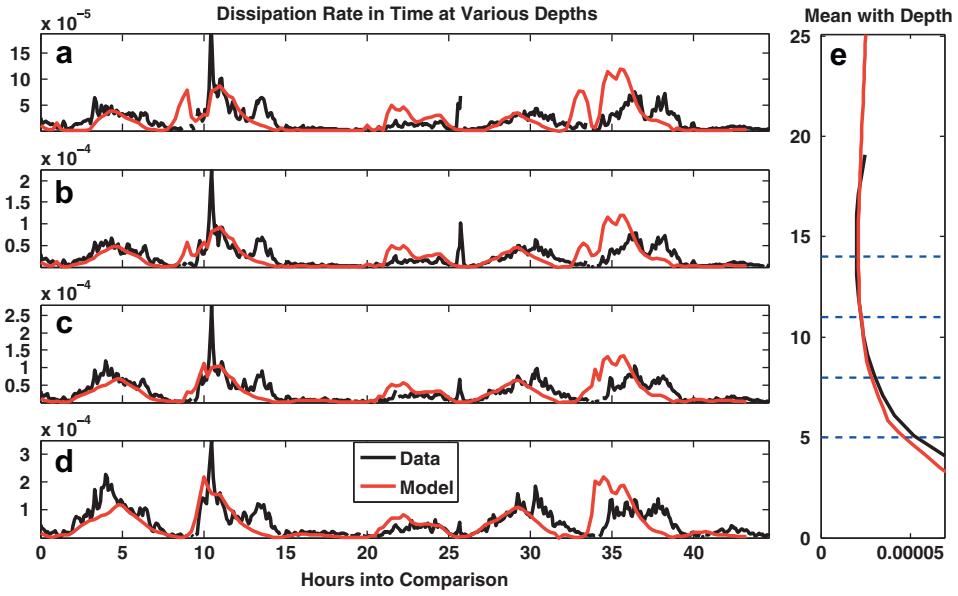

Fig. 8. Turbulent dissipation rate comparisons between data (black) and model output (red) at Admiralty Head for the same time as Fig. 7 but at multiple depths. The comparison depths are indicated, in order, as blue dashed lines on the time-mean profile of the turbulent dissipation rate profiles in Fig. 8. Fig. 8(c) is approximately at hub height. (For interpretation of the references to colour in this figure caption, the reader is referred to the web version of this article.)

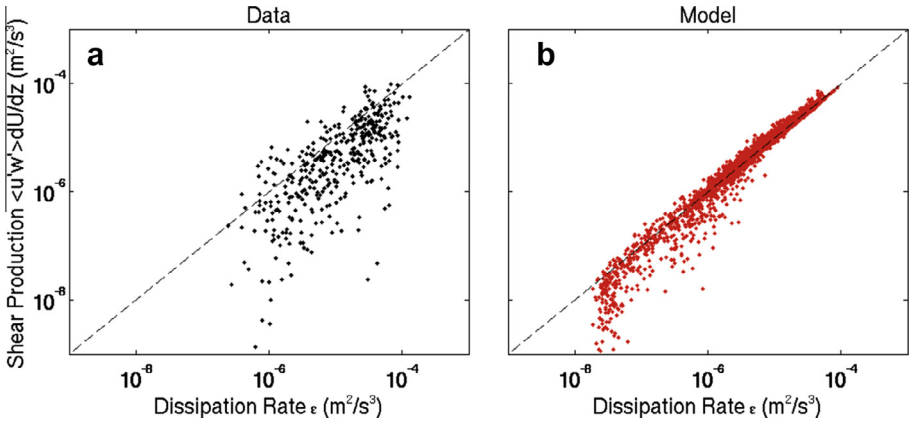

Fig. 9. Hub height shear production compared with dissipation rate at Nodule Point. Data is shown in Fig. 9(a) and and model output is in Fig. 9(b).

4. Analysis

Results from the previous section show that the turbulence model does fairly well at estimating the rate at which energy is being extracted from the resolved flow field; this energy extraction is equivalent to the turbulence production rate (Section 5.2.1). It also does fairly well at estimating the turbulence dissipation rate.

However, at Nodule Point it does not do well at estimating the measured turbulent kinetic energy. This is because, in addition to more classical type of turbulence, the data contain low-frequency, quasi-horizontal motions for which the turbulence models are not intended. The low-frequency, quasi-horizontal motions in the field data are not contained in the resolved-scale flow nor in the TKE_{model}. Of course with much higher resolution, we could resolve these scales of motion; however, resolving these motions is well beyond our present computer resources.

Here, using a good estimate of the turbulence dissipation rate obtained from the turbulence model, we can extrapolate into this low frequency range, which is unresolved in the numerical model, and obtain a significant improvement in our estimation of the measured turbulence. This post-processing approximation can then be used for applications such as tidal turbine siting or pollutant dispersal, for which accurate modeling requires an estimate of turbulent kinetic energy over a fuller frequency range.

4.1. Extrapolation of inertial sub-range

TKE_{obs} spectra calculated from ADV observations (Fig. 2) suggest the classic spectra shape of $f^{-5/3}$ (already adjusted from the original wavenumber form of $\kappa^{-5/3}$ as described earlier) is a good approximation at frequencies much lower than the roughly isotropic limit of 0.2 Hz. (This frequency limit is associated with the approximate largest vertical motion, determined by the water depth.) Some support for this approximation can be found for flows where the vertical velocity is suppressed by density stratification or by the free surface (see Section 5.3). Therefore, we approximate that the turbulent kinetic energy is related to frequency by $f^{-5/3}$ over not just the classical frequency range but over the larger range shown in Fig. 2. This will be referred to as the diagnostic turbulent kinetic energy, TKE_{diag}. We then use this data-informed, diagnostic method as an alternative calculation of the TKE_{model} supplied by the numerical model system (*i.e.*, the ROMS simulation) using the local

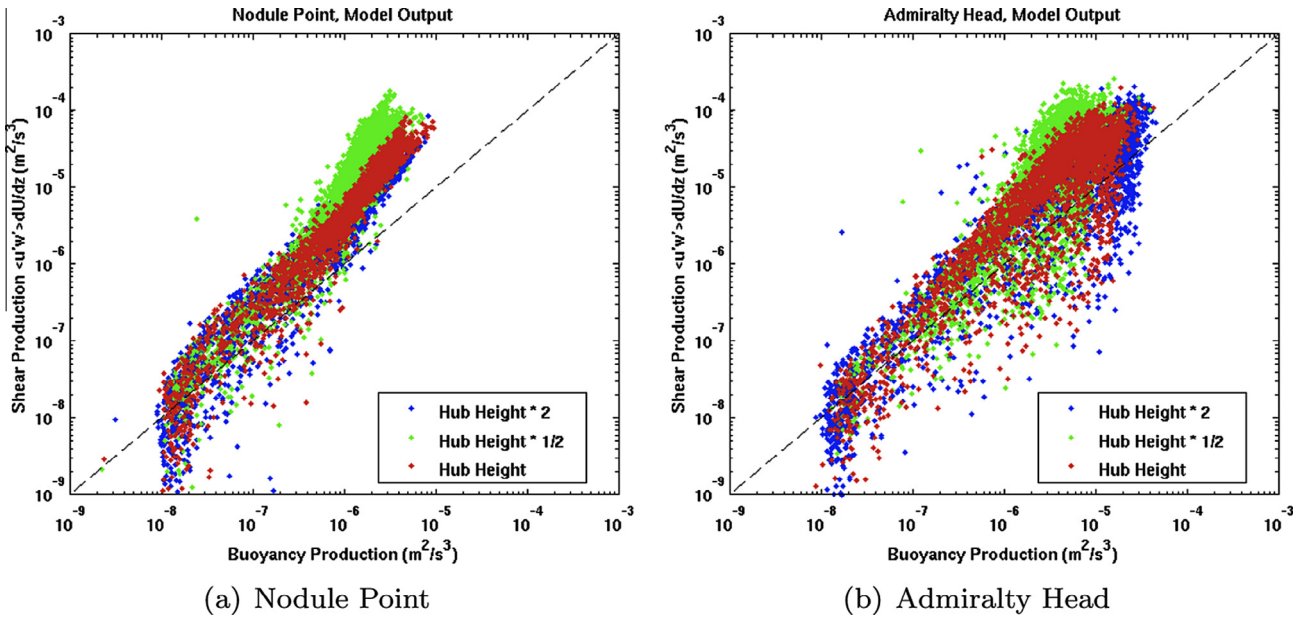

Fig. 10. Model shear production compared with buoyancy production at multiple depths. Because the buoyancy production is negative, the absolute value has been taken in order to plot on a logarithmic axis.

mean velocity and the turbulent dissipation rate, both directly output by the simulation. The idea is that while the k-ε closure scheme assumes the $f^{-5/3}$ relationship only over the classical range of frequencies, an improved representation of the turbulent kinetic energy in this case may be achieved by being informed by the data spectrum, which has different, but related, behavior. This relies on having a reasonable representation of the local velocity field and turbulent dissipation rate. Combined with relationships from Section 2.1, the TKE_{diag} over the frequency range shown for the data can be calculated via

$$k_{it} = \int_{\kappa_1}^{\infty} \alpha\varepsilon^{2/3}\kappa_i^{-5/3}\mathrm{d}\kappa + \int_{\kappa_1}^{\infty} \alpha\varepsilon^{2/3}\kappa_j^{-5/3}\mathrm{d}\kappa \tag{11}$$

$$= \int_{f_1}^{\infty} \alpha\varepsilon^{2/3}\left(\frac{2\pi f}{u}\right)^{-5/3}\frac{2\pi}{u}\mathrm{d}f + \int_{f_1}^{\infty} \alpha\varepsilon^{2/3}\left(\frac{2\pi f}{v}\right)^{-5/3}\frac{2\pi}{v}\mathrm{d}f$$

$$= \frac{\alpha}{(2\pi)^{2/3}}\varepsilon^{2/3}(u^{2/3}+v^{2/3})\int_{f_1}^{\infty} f^{-5/3}\mathrm{d}f$$

$$= \frac{\alpha}{(2\pi)^{2/3}}\varepsilon^{2/3}(u^{2/3}+v^{2/3})\left[-\frac{3}{2}f^{-2/3}\right]_{f_1}^{\infty}$$

$$= \frac{3}{2}\frac{\alpha}{(2\pi)^{2/3}}\varepsilon^{2/3}(u^{2/3}+v^{2/3})f_1^{-2/3}, \tag{12}$$

where $f_1 = 1/T_1$ is the lowest frequency included in the spectral analysis, $T_1 = 128$ s, $\alpha = 0.5$, and κ_i and κ_j are the wave numbers in the x- and y-directions. We also define this TKE_{diag} as "inferred total turbulent kinetic energy," k_{it}, from the model.

Eq. 12 gives an expression that approximates the energy contained in the model in both horizontal axes. This will be compared with both the along- and across-principal axis components of the TKE_{obs}. At hub height at Nodule Point, data is available for both components, and for all other comparisons, the across-principal axis TKE_{obs} component is included using the multiplier to the TKE_{obs} of 1.64 (discussed in Section 2.1).

4.2. Adjusted comparisons

Fig. 11 shows TKE comparisons at hub height at Nodule Point and Admiralty Head, including both the TKE_{model} (red) and TKE_{diag} (green), and both the classical (blue) and total (black) TKE_{obs}. The TKE_{diag} is in better agreement with the total TKE_{obs} at both sites, although the difference is less notable at Admiralty Head. As will be discussed in Section 5.1, the TKE_{model} and total TKE_{obs} at Admiralty Head may be closer together because of a broader inertial subrange at Admiralty Head (where the flow is more energetic and the water depth is greater).

Fig. 12 shows TKE comparisons at multiple depths at Nodule Point (Fig. 12(a–d)) with depths indicated in the time-mean plots of TKE with depth in Fig. 12(e). As before when showing dissipation rate with depth from the ADCP data, the TKE_{obs} estimated from the ADCP data are calibrated using a the ratio of the average ADV hub height value to the nearest ADCP depth mean value. The inferred TKE_{diag} matches well with the observed total TKE_{obs} nearest the seabed and improves the model-data comparisons throughout the water column. Farther above the seabed, the TKE_{diag} is still biased low relative to the observed total TKE_{obs}. This is consistent with the trend in dissipation rate $\varepsilon(z)$, which is used to estimate the TKE_{diag}.

Fig. 13 shows TKE comparisons at multiple depths at Admiralty Head. Fig. 13(c) is approximately at hub height. Though the TKE_{obs} and TKE_{model} values were already in rough agreement at Admiralty Head, the TKE_{diag} does improve the comparison with the TKE_{obs} at all selected depths. However, near the seabed (Fig. 13(d)), the TKE_{diag} is biased high. This may be expected since the TKE_{diag} is a function of the modeled turbulent dissipation rate, which is large near the seabed. For the purpose of tidal turbine siting using this model, a mismatch in values very near the seabed is acceptable since potential hub heights are higher in the water column.

Turbulence intensity using the TKE_{model} is calculated as shown in Section 2.5. A slightly different expression should be used for the case when using the TKE_{diag}, because it represents only the horizontal components of the turbulent kinetic energy instead of all three components. Therefore, the expression for turbulence intensity as calculated from the TKE_{diag} is given by

$$I = \frac{\sqrt{k_{it}}}{\sqrt{u^2+v^2}},$$

where TKE_{diag} or k_{it} approximately represents $\frac{1}{2}(\overline{u'^2}+\overline{v'^2}) \approx \overline{u'^2}$, the horizontal components of the turbulent kinetic energy.

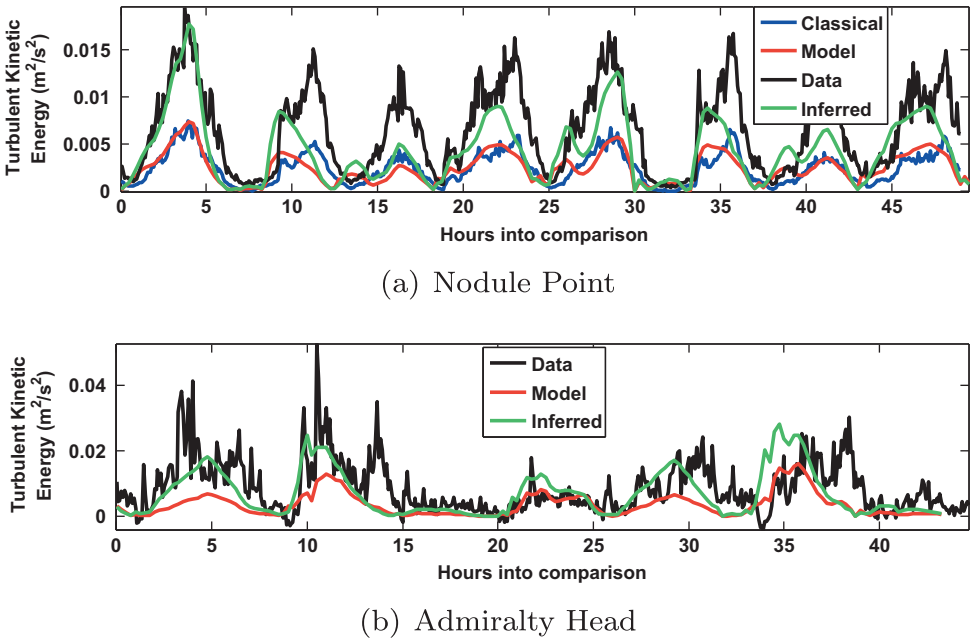

Fig. 11. Hub height time series comparison with inferred turbulent kinetic energy at Nodule Point and Admiralty Head. At Nodule Point, "classical" TKE_{obs} and "model" TKE_{model} turbulent kinetic energy include vertical and horizontal components, and "inferred" TKE_{diag} (model) and "data" TKE_{obs} turbulent kinetic energy include only horizontal energy. At Admiralty Head, all turbulent kinetic energy signals include only horizontal components.

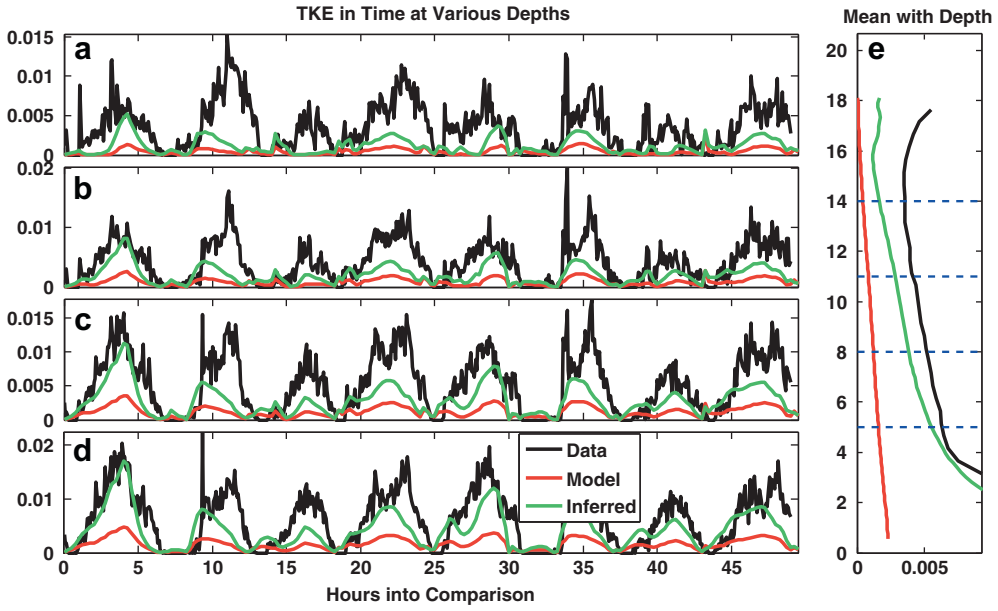

Fig. 12. TKE comparisons between data (black), model output (red), and inferred model calculation (green) at Nodule Point for the same time as Fig. 4, but at multiple depths. The comparison depths are indicated, in order, on the time-mean profile of the TKE profiles in Fig. 12(e) as blue dashed lines. All TKE values include only horizontal components. (For interpretation of the references to colour in this figure caption, the reader is referred to the web version of this article.)

Fig. 14(a) shows the turbulence intensity comparison for hub height at Nodule Point. Although there is poor correlation between the TKE_{model} predictions and the TKE_{obs}, the average of the TKE_{diag} and the average TKE_{obs} compare well. As expected, the TKE_{model} values are biased low compared with the observations. Despite the lack of correlation, the agreement in both mean and the spread of the values suggests that the TKE_{diag} turbulence intensities can be used as accurate statistical descriptions of the flow.

Fig. 14(b) shows the turbulence intensity comparison for Admiralty Head. The spread in both data and model output is larger at this location than at Nodule Point, but the comparison is similar. The inferred model values have the best agreement with the observed values.

5. Discussion

Implications and interpretations of the results of this study are discussed here. While previous studies and theory are incorporated to understand the results as best as possible, future work will be required to directly evaluate these hypotheses.

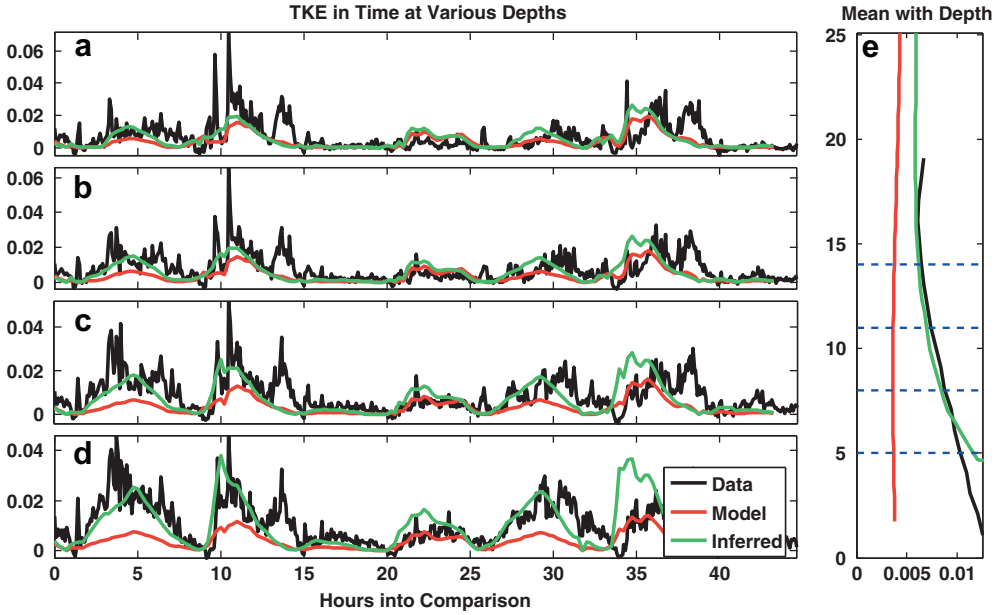

Fig. 13. TKE comparisons between data (TKE_{obs}, black), model output (TKE_{model}, red), and inferred model calculation (TKE_{diag}, green) at Admiralty Head for the same time as Fig. 4 but at multiple depths. The comparison depths in Fig. 13(a–d) are indicated, in order, on the time-mean profile of the turbulent kinetic energy profiles in Fig. 13(e) as blue dashed lines. All TKE values include only horizontal components. (For interpretation of the references to colour in this figure caption, the reader is referred to the web version of this article.)

5.1. Site differences

The comparisons of the TKE_{model} and TKE_{obs} differ for Nodule Point and Admiralty Head. At Admiralty Head, the TKE_{model} matches observations better than at Nodule Point. This may be related to a difference in the energy spectrum at each site. In the spectrum at Nodule Point, shown in Fig. 2, the data has a classical range from about $0.2 < f < 2$ Hz. It was also found that the model output compared well with turbulent kinetic energy in the classical range. If this is true at Admiralty Head as well, then the fact that the data-model comparison is better may imply that the classical range at this site spans a broader frequency range (see Fig. 15 for an illustration of this). The larger classical turbulence frequency range at Admiralty Head may be because it is a deeper site, allowing larger vertical scales (this is mentioned in Thomson et al., 2012). The larger depth at Admiralty Head could extend the band of frequencies included in the classical range out further into larger scales, improving the comparison between the model and data accordingly. This hypothesis has been tested using data from a June 2012 deployment of an ADV near Admiralty Head (described briefly in Section 2.1). Results support the hypothesis, but also indicate somewhat more complicated behavior at Admiralty Head.

The spectrum from Admiralty Head is shown in Fig. 16. Analogous to Nodule Point, the spectrum at Admiralty Head includes the same types of relative behavior between the horizontal and vertical components (approximately categorized here): quasi-horizontal behavior at low frequencies ($f < 0.04$ Hz), Doppler noise

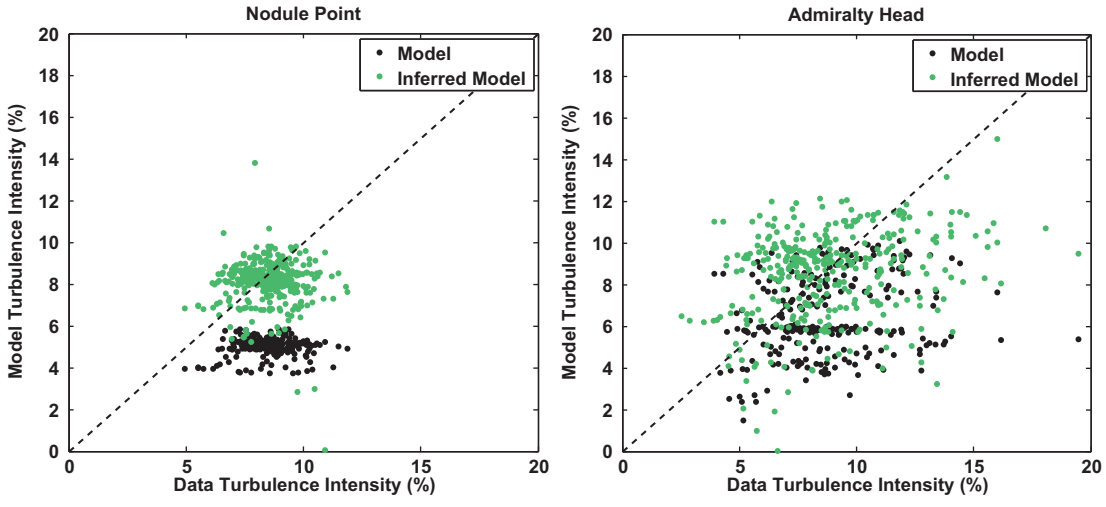

(a) Nodule Point (b) Admiralty Head

Fig. 14. Turbulence intensity comparison between ADV data, model output, and inferred model output at hub height of 4.7 meters at Nodule Point and 8.1 meters at Admiralty Head. The time periods used are the same as in previous comparisons.

dominating the signal at high frequencies ($f > 1$ Hz), and a range in the middle frequencies in which the vertical and horizontal components are comparably-sized and approximately follow the $f^{-5/3}$ relationship ($0.3 < f < 1$ Hz). There is a second middle-range categorization of behavior indicated on the spectrum: a transition region ($0.04 < f < 0.3$) between quasi-horizontal and classical behavior. In this region, the horizontal and vertical components of TKE are similar in magnitude, but they together trend away from the $f^{-5/3}$ relationship. This transition occurs subtly over a wide range of frequencies. Together, the two middle frequency ranges form a larger region of approximately classical turbulence than was seen at Nodule Point.

The depth at the Nodule Point data site, which was around 20 meters, was explained as being the controlling length scale for the behavior of the vertical component of energy density. At the Admiralty Head ADV location, the depth was 55 meters, and we expect this larger depth to increase the range of frequencies included in the roughly classical turbulence range. This is what we see in Fig. 16. The vertical component diverges from the horizontal component at a lower frequency than at Nodule Point. Also, in the larger range of frequencies between this point and the high frequency at which Doppler noise dominates, the components behave roughly as classical turbulence. While the behavior seen here may contain some motion contamination from the mooring, it may be evidence of the fact that while the data location itself is deeper than at Nodule Point, the bathymetry is also more complex, and no single length scale limits the vertical eddies.

We previously found that when the spectral energy density at Nodule Point was limited to frequencies corresponding to three-dimensional turbulent behavior, the TKE_{model} and TKE_{obs} compared reasonably well. This implied that the model may capture three-dimensional classical turbulence well, in this particular flow environment. It was speculated that, based on our understanding of the physics at Nodule Point, the model would capture more of the full TKE_{obs} at deeper Admiralty Head, since more of the energy would be contained in the larger expected classical frequency range. This was the case in the previous comparison at Admiralty Head and is found to be the case in the time series associated with the spectrum in Fig. 16 (not shown).

5.2. Model performance

5.2.1. Description of model spectrum

There may appear to be an inconsistency in the presented results: the turbulent dissipation rate and Reynolds stresses from the model compare reasonably well with the data, but the turbulent kinetic energy does not. This section addresses some of the relevant nuances.

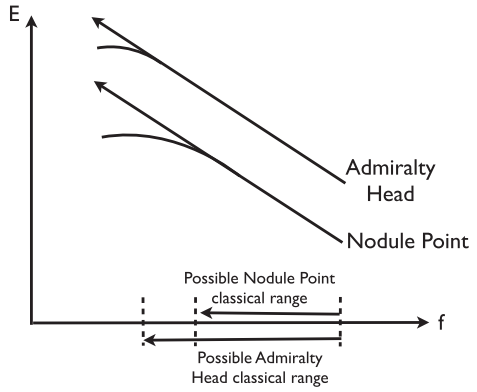

Fig. 15. Possible explanation for the difference in energy comparisons at Nodule Point and Admiralty Head between data and model. It is possible that the inertial subrange at Admiralty Head extends to lower frequencies than at Nodule Point, so that the turbulence closure scheme is able to describe a greater fraction of the total energy.

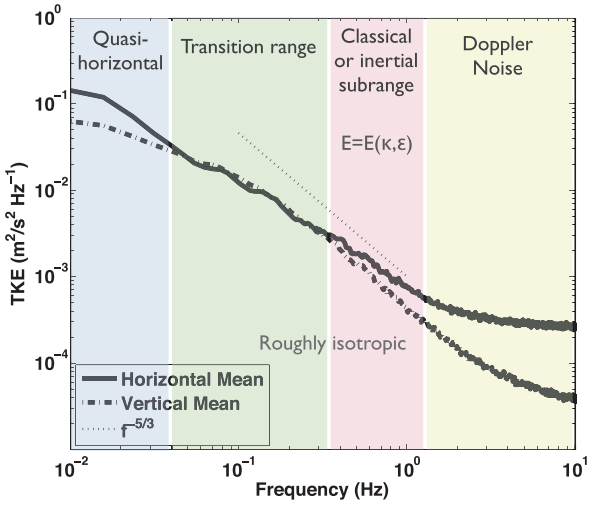

Fig. 16. ADV spectral energy density at Admiralty Head. The mean horizontal component of the spectrum is shown as a solid line and the mean vertical component is dash-dot. A line representing $f^{-5/3}$ is also shown for comparison.

The rate of loss of the computed-scale kinetic energy in the model is equal to the shear production rate in the governing equation for the turbulent kinetic energy (Eq. 9). That is, the kinetic energy lost from the mean flow is gained by the turbulence dynamics, and thus it is important that the production term is approximately right in the simulations. The turbulence dissipation rate is related to the turbulence production rate, as shown from the simulation results and from the data, so the fact that the dissipation rate ε is approximately correctly predicted at both sites is reassurance that the proper amount of kinetic energy is being removed from the computed flow field.

However, while the turbulent dissipation rate is modeled based on the classical range in the turbulence closure scheme, the turbulent kinetic energy is sensitive to the scales included in the data or model. We consider the classical range-only TKE_{obs} to be a fair comparison with what the TKE_{model} represents and, in this regard, the model performs relatively consistently across turbulence fields when compared with the data. Because the TKE_{obs} includes a broader range of scales than the model is intended for, and we are interested in matching this range for our application, we extend theory to try to account for the difference.

An interpretation of the behavior seen in the data spectrum is that larger flow features (at lower frequencies) may not participate in the local production-dissipation balance and energy cascade, but rather just advect through (Thomson et al., 2012). Thus, the model and data can be consistent at small scales and in terms of a cascade, even if the model does not resolve intermediate scales (between the mean flow and the classical range). The speculative argument made in Section 5.3, implying the spectrum only depends upon wave number and epsilon in the large-scale TKE range, implies, like Kolmogorov's inertial range theory, that TKE is transferred through this range, but that it is not produced or not dissipated, which would be consistent with the energy production occurring at the larger, resolved scales of motion.

5.2.2. Regarding speed deficiency

There is a known horizontal speed deficiency in the model such that the modeled mean speed is on average about 75% of the observed mean speed, due to the low M_2 tide inherited from the

forcing model. This can be seen for Nodule Point in the speed comparison in Fig. 4. This deficiency is expected to carry over to the turbulence values, which are indeed shown to be biased low relative to the observations. In the particular time series comparison at Nodule Point, the speed predicted by the model, averaged over the time series, is 78% the value of the speed found in the field data.

Dimensional analysis suggests that TKE should scale approximately with the square of the current speed. The horizontal components of the TKE predicted by the original k-ε model, TKE_{model}, for this time period, at hub height, are, on average, about 25% the size of the horizontal components of the turbulent kinetic energy from the field data, TKE_{obs}. This is lower than the deficiency in TKE that is expected, based on a scaling with velocity squared, which would give $0.78^2 = 0.61$. However, as is discussed in Section 3.1, the TKE_{model} is limited to the classical turbulence range, whereas the TKE_{obs} includes energy from a larger frequency range. Thus, there are two distinct sources of the deficiency for the TKE_{model}: less energy in the system due to a speed deficiency, and the limited intended frequency range of the turbulence model. In Section 4, an approximation is made to infer the energy in the model over a larger frequency range of the turbulent spectrum than in the turbulence model itself, to find TKE_{diag}. This calculation has improved agreement with the TKE_{obs} for the horizontal TKE, such that the TKE_{diag} values are, on average, about 84% the of the TKE_{obs} values. The TKE_{diag} is still low relative to the TKE_{obs} due to the remaining speed deficiency in the system.

The turbulent dissipation rate is expected to scale approximately with the cube of the speed, according to classical turbulence theory (Pope, 2000). This is close to what is seen in the comparison: the model prediction of the dissipation rate is about 56% the size of the field data dissipation rate (as measured by a time-average at hub height of each quantity), a little larger than the direct cube of the model speed size relative to the data, $0.78^3 = 0.47$. Thus, the turbulent dissipation rate predicted by the model is low compared with the field data by a factor of about two, and this is roughly consistent with the known speed deficiency in the model.

5.3. Shape of the turbulence spectrum

The ADV spectra from Nodule Point (Fig. 2) show a region of classical isotropic turbulence in the middle frequency range and quasi-horizontal motion in the lower frequency range. In addition, the figure shows that the inertial range behavior with a $-5/3$ spectrum extends from the classical turbulence range well into the lower-frequency, quasi-horizontal range. In this section we speculate on the reasons for this latter behavior, which is inconsistent with Kolmogorov's classical arguments.

Quasi-horizontal behavior in the lower-frequency range, together with inertial range spectral behavior, has been observed in other cases. For example, in a shallow tidal river system near the Puget Sound, the energy density spectrum has been found to have a similar inertial-range shape (Chickadel et al., 2011), *i.e.*, approximately isotropic, inertial range behavior at horizontal scales of the order of the depth from the free surface, but with the inertial range continuing up to horizontal scales well beyond the depth of the the measurement. In this situation, the vertical motions are probably suppressed by the close proximity of the measurements to the river surface, which remains relatively flat due to gravity and to light wind conditions. Interestingly, in this case 'boils' from below advect momentum towards the free surface at the horizontal scale of the larger-scale motion. In a coastal inlet, Dugan and Piotrowski (2012) made measurements of the horizontal spectral energy density at the water surface of a shallow tidal channel. In this case the vertical velocity is probably suppressed at horizontal scales above the depth of the channel, leading to the same argument as for the Nodule Point case. Some of their results indicate inertial range behavior at horizontal scales larger than the depth of the channel, consistent with the Nodule Point results. In a series of numerical simulations of a strongly stratified fluid, Lindborg (2006) found similar inertial range behavior in the horizontal spectra, in this case with stable density stratification inhibiting the vertical velocity at larger horizontal scales. In strongly stratified flows, at horizontal length scales larger than the Ozmidov (overturning) scale, vertical motion is suppressed by the stable density stratification, so the flow is quasi-horizontal, but again with vertical shear. Lindborg hypothesized that an anisotropic, downscale energy cascade was occurring; at horizontal scales above the classic inertial range and Ozmidov scales, he argued that the horizontal spectra would depend only on the horizontal wave number and the energy transfer rate, i.e., the kinetic energy dissipation rate, leading to the $-5/3$ result.

All of these situations suggest that when there is a physical mechanism limiting the vertical component of motion, there can exist quasi-horizontal motions at frequencies (horizontal wave numbers) lower than the classical turbulence range and that these motions can have inertial range behavior. The energy in this range may therefore follow the $f^{-5/3}$ trend; however the arguments for this inertial range region are different from Kolmogorov's classical theory, since in this range the vertical motion is suppressed so that the flow is strongly anisotropic (see Section 2.1).

There are other functions that could be used to approximate the TKE spectrum at lower frequencies. The data in the spectrum starts to roll off at the lowest frequencies in the measurements (Fig. 2), such that the $f^{-5/3}$ relationship becomes an overestimate at those frequencies. In Walter et al. (2011), other estimates of energy density data were found using Kaimal curves. These are consistent with with $f^{-5/3}$ behavior at frequencies below the isotropic range, but then reproduce the roll-off at the even lower frequencies seen in the data, and were found to be more appropriate in locations that are limited by depth, as in Admiralty Inlet. This could be attempted in the future.

5.4. Application to tidal turbine siting

For wind and tidal turbine siting, a commonly-used turbulence metric for assessing a site is turbulence intensity, as described in Section 2.5. Turbulence intensity at hub height for Nodule Point (Fig. 14(a)) and and from Admiralty Head (Fig. 14(b)) both compared well between the inferred model output and the data.

Table 1 summarizes the mean values in time of the turbulence intensity at each location, and gives further evidence that the inferred calculation for the turbulence intensity gives a good estimate of the measured values. Fig. 17 shows the distribution of hub-height TKE_{model} (using the inferred calculation) throughout the model domain. Turbulence is elevated near headlands and topographic features (sills), and thus these locations may be less suitable for turbine placement.

Both turbulence intensity and total TKE integrate over a wide spectrum of scales. However, there is evidence that not all turbulent length scales have the same effect on a turbine. In one study, researchers found that increasing the turbulence intensity increased the load on a wind turbine, but they also found that decreasing the length scale while holding the kinetic energy fixed increased the load (Thomsen and Sørensen, 1999). It is possible that it is actually the smaller, higher frequency motions that are most detrimental to a turbine, though presumably this would also depend on the specific turbine design characteristics. These are the scales of motion in the classical range, and that appear to be most accurately captured by the turbulence closure model examined here. In this regard, it may be helpful to consider a turbine siting metric that includes energy from only smaller length scales/higher

Table 1
Average turbulence intensity values for the comparison time periods from the data and the model output.

	I, Data (%)	I, Model (%)	I, Inferred Model (%)
Nodule Point	8.5	4.9	8.3
Admiralty Head	8.8	6.1	8.8

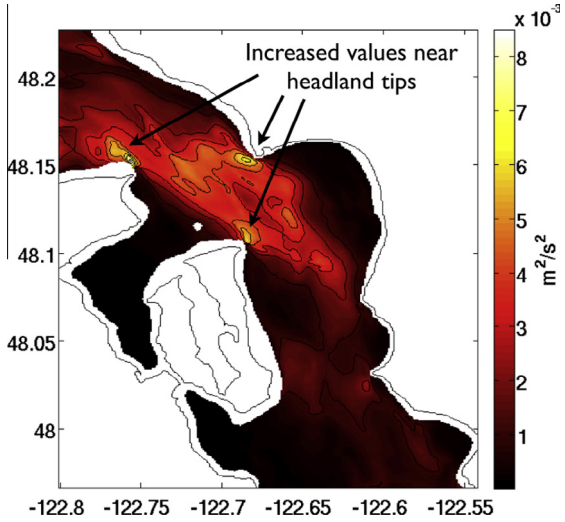

Fig. 17. Mean TKE_{diag} at hub height throughout Admiralty Inlet. Largest values are seen primarily near headlands.

frequencies/larger wave numbers, as the most relevant measure for a turbine. One such metric, the fractional turbulence intensity, which gives the turbulence intensity as a function of length scale, has been suggested (Thomson et al., 2012).

6. Summary

Model-data comparisons are shown here between output from a high resolution model of Admiralty Inlet, employing a two-equation k-ε turbulence closure scheme, and high-quality turbulence measurements at two locations within Admiralty Inlet. The comparisons emphasize the model performance at hub height in order to understand how well the model performs at the depth that pertains most to siting tidal turbines. The modeled turbulent dissipation rate, Reynolds stress, and classical TKE are consistent with measurements. The turbulent dissipation rate and Reynolds stress from the model prediction are lower than the data values but within a factor of two, and this performance indicates that the approximately correct amount of energy is being extracted from the mean flow to be input into the turbulence dynamics. The deficiency in the model prediction of these quantities can partially be explained by the known speed deficiency in the larger-scale simulation results into which the present simulation was embedded.

Given relatively accurate model values for the horizontal speed and the dissipation rate from the turbulence closure scheme, the amplitude of the TKE frequency spectrum in the classical $f^{-5/3}$ range can be inferred. Extrapolating this portion of the spectrum to lower frequencies, following the anisotropic behavior seen in the data energy density spectrum, provides an improved, diagnostic estimate of the total TKE over a wider range of frequencies.

Disclaimer

This report was prepared on an account of work sponsored by an agency of the United States Government. Neither the United States Government nor any agency thereof, nor any of their employees, makes any warranty, expressed or implied, or assumes any legal liability or responsibility for the accuracy, completeness, or usefulness of any information, apparatus, product, or process disclosed, or represents that is use would not infringe privately owned rights. Reference herein to any specific commercial product, process, or service by trade name, trademark, manufacturer, or otherwise does not necessarily constitute or imply its endorsement, recommendation, or favoring by the United States Government or any agency thereof. Their views and opinions of the authors expressed herein do not necessarily state or reflect those of the United States Government or any agency thereof.

Acknowledgments

Thanks to Parker MacCready and David Sutherland for providing access to their regional model output as well as aid in the nesting process. Thanks also to Sarah Giddings for helpful conversations about the nature of turbulence and turbulence modeling, the MoSSea Users Group for ideas and support, and to Joe Talbert, Alex deKlerk, and Capt Andy Reay-Ellers who helped with the data collection. This paper was improved based on helpful suggestions from reviewers. This material is based upon work supported by the Department of Energy under Award Number DE-FG36-08GO18179 and by the University of Washington PACCAR Professorship.

References

Beckmann, A., Haidvogel, D.B., 1993. Numerical simulation of flow around a tall, isolated seamont. Part I: Problem formulation and model accuracy. Journal of Physical Oceanography 23, 1736–1753.
Chickadel, C., Talke, S.A., Horner-Devine, A.R., Jessup, A.T., 2011. Infrared-based measurements of velocity, turbulent kinetic energy, and dissipation at the water surface in a tidal river. IEEE Geoscience and Remote Sensing Letters 8 (5), 849–853.
Dugan, J.P., Piotrowski, C.C., 2012. Measuring currents in a coastal inlet by advection of turbulent eddies in airborne optical imagery. Journal of Geophysical Research 117 (C3), C03020.
Frandsen, S., 2007. Turbulence and turbulence-generated structural loading in wind turbine clusters. PhD thesis, Risø National Laboratory.
Galperin, B., Kantha, L.H., Hassid, S., Rosati, A., 1988. A quasi-equilibrium turbulent energy model for geophysical flows. Journal of the Atmospheric Sciences 45 (1), 55–62.
Haas, K.A., Fritz, H.M., French, S.P., Smith, B.T., Neary, V., 2011. Assessment of energy production potential from tidal streams in the United States. Technical Report, Georgia Tech Research Corporation, NA.
Haidvogel, D.B., Arango, H., Budgell, W.P., Cornuelle, B.D., Curchitser, E., Lorenzo, E.D., Fennel, K., Geyer, W.R., Hermann, A.J., Lanerolle, L., 2008. Ocean forecasting in terrain-following coordinates: formulation and skill assessment of the regional ocean modeling system. Journal of Computational Physics 227 (7), 3595–3624.
Haney, R.L., 1991. On the pressure gradient force over steep topography in sigma coordinate ocean models. Journal of Physical Oceanography 21, 610–619.
Kawase, M., Thyng, K.M., 2010. Three-dimensional hydrodynamic modelling of inland marine waters of Washington State, United States, for tidal resource and environmental impact assessment. IET Renewable Power Generation 4 (6), 568–578.
Lindborg, E., 2006. The energy cascade in a strongly stratified fluid. Journal of Fluid Mechanics 550 (1), 207.
Madsen, P.H., Frandsen, S., 1984. Wind-induced failure of wind turbines. Engineering Structures 6 (4), 281–287.
Maganga, F., Germain, G., King, J., Pinon, G., Rivoalen, E., 2010. Experimental characterisation of flow effects on marine current turbine behaviour and on its wake properties. Renewable Power Generation, IET 4 (6), 498–509.
Mofjeld, H.O., Larsen, L.H., 1984. Tides and tidal currents of the inland waters of western Washington. Technical Report, National Oceanic and Atmospheric Administration.
NNMREC, University of Washington, 2010. Northwest National Marine Renewable Energy Center.
Polagye, B., Bedard, R., Previsic, M., 2007. Tidal in-stream energy conversion survey and characterization of SnoPUD project sites in Puget Sound. Technical Report EPRI-TP-003, EPRI technical report, WA.
Pope, S.B., 2000. Turbulent Flows. Cambridge University Press.
Previsic, M., Bedard, R., Polagye, B., 2008. System level design, performance, cost and economic assessment – Admiralty Inlet, Washington tidal in-stream power

plant 2008 update. Technical Report EPRI-TP-006 SnoPUD Rev. 1, EPRI technical report, WA.
Seim, H.E., Gregg, M.C., 1995. Energetics of a naturally occurring shear instability. Journal of Geophysical Research 100 (C3), 4943–4958.
Shchepetkin, A.F., McWilliams, J.C., 2005. The regional ocean modeling system (ROMS): a split-explicit, free-surface, topography-following coordinates ocean model. Ocean Modelling 9 (4), 347–404.
Sheinman, Y., Rosen, A., 1992. A dynamic model of the influence of turbulence on the power output of a wind turbine. Journal of Wind Engineering and Industrial Aerodynamics 39 (1–3), 329–341.
Simpson, J.H., Burchard, H., Fisher, N.R., Rippeth, T.P., 2002. The semi-diurnal cycle of dissipation in a ROFI: model-measurement comparisons. Continental Shelf Research 22, 1615–1628.
Stacey, M.T., Monismith, S.G., Burau, J.R., 1999. Observations of turbulence in a partially stratified estuary. Journal of Physical Oceanography 29 (8), 1950–1970.
Stips, A., Burchard, H., Bolding, K., Eifler, W., 2002. Modelling of convective turbulence with a two-equation k-ε turbulence closure scheme. Ocean Dynamics 52 (4), 153–168.
Sutherland, D.A., MacCready, P., Banas, N.S., Smedstad, L.F., 2011. A model study of the Salish Sea estuarine circulation. Journal of Physical Oceanography 41 (6), 1125–1143.
Taylor, G.I., 1938. The spectrum of turbulence. Proceedings of the Royal Society, Series A 164, 476–490.
Thomsen, K., Sørensen, P., 1999. Fatigue loads for wind turbines operating in wakes. Journal of Wind Engineering and Industrial Aerodynamics 80 (1), 121–136.
Thomson, J., Kilcher, L., Richmond, M., Talbert, J., deKlerk, A., Polagye, B., Guerra, M., Cienfuegos, R., 2013. Tidal turbulence spectra from a compliant mooring. In: Proceedings of the 1st Marine Energy Technology, Symposium (METS2013).
Thomson, J., Polagye, B., Durgesh, V., Richmond, M.C., 2012. Measurements of turbulence at two tidal energy sites in Puget Sound WA. IEEE Journal of Oceanic Engineering 37 (3), 363–374.
Thyng, K.M., 2012. Numerical Simulation of Admiralty Inlet, WA, with Tidal Hydrokinetic Turbine Siting Application. PhD Thesis, University of Washington.
Umlauf, L., Burchard, H., 2003. A generic length-scale equation for geophysical turbulence models. Journal of Marine Research 61, 235–265.
Wagner, R., Courtney, M.S., Larsen, T.J., Paulsen, U.S., 2010. Simulation of shear and turbulence impact on wind turbine performance. Technical Report, Risø National Laboratory for Sustainable Energy Technical, University of Denmark.
Walter, R.K., Nidzieko, N.J., Monismith, S.G., 2011. Similarity scaling of turbulence spectra and cospectra in a shallow tidal flow. Journal of Geophysical Research 116 (C10), C10019.
Wang, B., Giddings, S.N., Fringer, O.B., Gross, E.S., Fong, D.A., Monismith, S.G., 2011. Modeling and understanding turbulent mixing in a macrotidal salt wedge estuary. Journal of Geophysical Research 116 (C2), C02036.
Warner, J.C., Geyer, W.R., Lerczak, J.A., 2005. Numerical modeling of an estuary: a comprehensive skill assessment, 110 (C05001) <darchive.mblwhoilibrary.org>.
Warner, J.C., Sherwood, C.R., Arango, H.G., Signell, R.P., 2005b. Performance of four turbulence closure models implemented using a generic length scale method. Ocean Modelling 8 (1–2), 81–113.